High-throughput compositional screening of $Pd_xTi_{1-x}H_y$ and $Pd_xNb_{1-x}H_y$ hydrides for CO_2 reduction

Ai, Changzhi; Chang, Jin Hyun; Tygesen, Alexander Sougaard; Vegge, Tejs; Hansen, Heine Anton

Published in:
ChemSusChem

Link to article, DOI:
10.1002/cssc.202301277

Publication date:
2024

Document Version
Early version, also known as pre-print

High-throughput compositional screening of $Pd_xTi_{1-x}H_y$ and $Pd_xNb_{1-x}H_y$ hydrides for CO_2 reduction

Changzhi Ai[†], Jin Hyun Chang[†], Alexander Sougaard Tygesen[†], Tejs Vegge[†], and Heine Anton Hansen[*†]

Abstract

Electrochemical experiments and theoretical calculations have shown that Pd-based metal hydrides can display good performance in the CO_2 reduction reaction (CO_2RR). To explore higher-performance catalysts, Pd-based alloy hydrides $Pd_xM_{1-x}H_y$ are studied in this work. Our previous work on doped-PdH showed that doping Ti and Nb into PdH can improve the CO_2RR activity, suggesting that the Pd alloy hydrides with better performance are likely to be found in the $Pd_xTi_{1-x}H_y$ and $Pd_xNb_{1-x}H_y$ phase space. However, the complex nature of the compositional and structural phase space that includes different compositions of alloy hydrides, different concentrations of the metal element and H of alloy hydrides, different adsorption sites, and different adsorbates, makes it intractable to screen out the stable and active $Pd_xM_{1-x}H_y$ catalysts using density functional theory (DFT) calculation. Herein, an active learning cluster expansion (ALCE) surrogate model equipped with Monte Carlo simulated annealing (MCSA), a CO* filter and a kinetic model are used to identify promising $Pd_xTi_{1-x}H_y$ and $Pd_xNb_{1-x}H_y$ catalysts with high stability and superior activity. Finally, 24 stable and active candidates of $Pd_xTi_{1-x}H_y$ and 6 active candidates of $Pd_xNb_{1-x}H_y$ are found using our approach. Among them, the $Pd_{0.23}Ti_{0.77}H$, $Pd_{0.19}Ti_{0.81}H_{0.94}$ and $Pd_{0.17}Nb_{0.83}H_{0.25}$ display superior current densities of approximately 5.1, 5.1 and 4.6 $\mu A\,cm^{-2}$ at -0.5 V overpotential, respectively, which are significantly higher than that of PdH at 3.7 $\mu A\,cm^{-2}$. Their free energy diagram shows that their HOCO* binding is not too weak, while their CO* binding is not too strong, resulting in enhanced activities. The statistical analysis shows that the binding energies are mainly contributed by the elements Ti/Nb and H. Hence, three candidates, $Pd_{0.23}Ti_{0.77}H$, $Pd_{0.19}Ti_{0.81}H_{0.94}$, and $Pd_{0.17}Nb_{0.83}H_{0.25}$, are recommended in this work.

[*]Corresponding author

Email: heih@dtu.dk

[†]Department of Energy Conversion and Storage, Technical University of Denmark, Anker Engelunds Vej, 2800 Kgs. Lyngby (Denmark)

1 Introduction

Current society still relies heavily on fossil fuels, which results in excessive carbon dioxide (CO_2) emissions. CO_2 is the primary greenhouse gas that causes weather anomalies and global warming.[1,2] Therefore, it is crucial to mitigate CO_2 emissions through various new technologies. On the one hand, it is possible to capture CO_2 that arises from the combustion of fossil fuels and from industries and then sequestrate it in an alternative geological formation.[3] On the other hand, CO_2 can be transformed into valuable fuels and chemicals via catalytic approaches, such as photocatalysis and electrocatalysis. Electrochemical CO_2 reduction reaction (CO_2RR) shows great potential to valorize CO_2 as useful fuels or chemicals.[3–5] The utilization of renewable energy sources such as wind and solar energy is gradually increasing to generate electricity, and the utilization cost is decreasing. However, there are still significant challenges for storing the generated electrical energy.[6,7] To face the challenges, the electrochemical CO_2 reduction is one of the most effective approaches via converting the generated electric energy to chemical energy carriers, such as carbon monoxide (CO), methane (CH_4), ethylene (C_2H_4), ethanol (C_2H_5OH) and propanol (C_3H_7OH).[3,8,9] This is an elegant solution that not only decreases the greenhouse effect but also obtains hydrocarbon chemicals when coupled with the utilization of renewable electricity. However, due to the chemical inertness of CO_2, it is very challenging to reduce CO_2 as it requires both energy input and favorable catalysts. Stability, activity, and selectivity of catalysts during the electrochemical process should be considered.[10]

Pure transition metal catalysts are usually stable and active for CO_2RR at room temperature, but their selectivities are quite different. Pure metal catalysts can be grouped into four categories based on their selectivity: (I) Cu is classified as its own category because it is the only metal that can simultaneously reduce CO_2 to multiple hydrocarbons and multi-carbon products such as CH_4, C_2H_4 and C_3H_7OH.[8,11–13] (II) Pb, Hg, Tl, and In are most likely to produce formate ($HCOO^-$) and the Faradaic efficiency of the products are over 90 %.[3] (III) Ni, Fe, Pt, and Ti produce H_2 without producing or producing only a very small amount of hydrocarbons (the Faradaic efficiency of H_2 over 90 %) via hydrogen evolution reaction (HER).[3] (IV) Au, Ag, Zn and Pd mainly reduce CO_2 to carbon monoxide (CO). It is worth pointing out that Pd can also produce an almost equal proportion of H_2 while producing CO.[13] We note that both CO and $HCOO^-$ are 2-electron products from CO_2RR, while CH_4, C_2H_4 and C_3H_7OH are 8-, 12- and 18-electron products, respectively.[14] CO and $HCOO^-$ have the shortest reaction pathways, and their energy conversion efficiencies can be very high. On the other hand, the pathways of the higher number of electron products are long, and their conversion efficiencies are usually very low. This is because a long reaction pathway makes the process complex and arduous to manipulate.[9] The conversion efficiency of CO_2RR for synthesizing multiple electron products C2 and C3, in particular, is far from the level viable for practical productions due to the consumption of a lot of electrons and protons and long pathways.[9,15] In contrast, the Faradaic efficiencies of 2-electron products CO or

$HCOO^-$ are usually higher than other products due to the short reaction pathways. Compared to liquid $HCOO^-$, CO is a gas that is easier to separate, and thus, reducing CO_2 to CO appears to be more achievable.

Though the Faradaic efficiency for CO formation of Pd is lower than that of Au, Ag, and Zn, Pd can simultaneously generate H_2 at a similar Faradaic efficiency due to the competitive HER. The generated CO and H_2 are the main components of syngas, which can be directly used to synthesize valuable chemical products via the Fischer–Tropsch processes.[3] Several works report that Pd-based catalysts can also produce syngas through electrochemical CO_2RR. Sheng et al. report that carbon-supported Pd nanoparticles (Pd/C) can simultaneously generate syngas with a CO to H_2 ratio between 0.5 and 1.[16] The current density can reach $0.6\,mA\,cm^{-2}$ at $-0.7\,V$ overpotential vs. reversible hydrogen electrode (RHE). In this electrochemical process, metal Pd nanoparticles are transformed into Pd hydride (PdH) as observed by in-situ X-ray absorption spectroscopy and in-situ X-ray diffraction. Density functional theory (DFT) calculation showed that PdH weakens the binding energies of both CO* and H*.[16] Zhu et al.[17] illustrated that different facets of Pd nanoparticles have an influence on their performance in CO_2RR to syngas; for example, Pd(111) surface has a higher activity of CO_2RR and better CO selectivity than the Pd(100) surface. The CO partial current density of PdH(111) in their work can reach $17\,mA\,cm^{-2}$ at $-0.7\,V$ overpotential vs. RHE, while that of PdH(100) is around $3\,mA\,cm^{-2}$, which is greater than that of commercial Pd catalysts. DFT calculation explains that forming PdH(111) makes CO* desorption no longer difficult and thus improves the activity of CO_2RR.[17]

Liu et al.[18] reported that Pd-modified niobium nitride (Pd/NbN) can produce a much higher partial current density of syngas and larger CO Faradaic efficiency than Pd-modified vanadium nitride (Pd/VN) catalyst and commercial Pd/C catalyst. Among them, the CO partial current density of Pd/NbH is the highest at around $0.7\,mA\,cm^{-2}$ at $-0.7\,V$ vs. RHE. In-situ X-ray diffraction illustrated the formation of PdH in Pd/NbN, which weakens *CO desorption and enhances the CO_2 conversion to syngas.[18] Lee et al.[19] reported the use of Pd-based bimetallic hydrides for producing syngas using electrochemical CO_2RR approach. The second metal, such as Co, Ni, Cu, Ag, and Pt, was chosen to form alloys with precious metal Pd nanoparticles and concentrations of the second metals were fixed at 25 % in their work. After applying potentials, the CoPd, NiPd, CuPd, AgPd, and PtPd alloys were transformed to (CoPd)H, (NiPd)H, (CuPd)H, (AgPd)H, and (PtPd)H, respectively, and their potentials of alloy hydrides formation were -0.322, -0.352, -0.434, -0.544 and $-0.544\,V$ vs. RHE, respectively. (AgPd)H, (CuPd)H, (NiPd)H, and (CoPd)H show higher CO partial current density than that of PdH. According to their CO/H_2 ratio, (CuPd)H and (NiPd)H are more suitable to produce syngas with the ratio range between 1 and 2.[19] Our previous study[20] using DFT suggested that among the transition metals Sc, Ti, V, Cr, Mn, Fe, Co, Ni, Cu, Zn, Y, Zr, Nb, Mo, Ru, Rh, Ag, Cd, Hf, Ta, W, and Re doped into PdH(111) at different doping configurations, Ti and Nb doping yielded a higher performance

of CO_2RR than undoped PdH(111). Furthermore, their generated CO and H_2 are suitable for generating syngas.[20] This gives clear guidance to further study of Ti- and Nb-Pd alloy hydrides.

In this work, $Pd_xTi_{1-x}H_y(111)$ and $Pd_xNb_{1-x}H_y(111)$ alloy hydrides are systematically studied via a hierarchy of theoretical calculations. Due to the vast search space of composition of $Pd_xTi_{1-x}H_y$ and $Pd_xNb_{1-x}H_y$, their stabilities are first explored by an active learning cluster expansion model equipped with Monte Carlo simulated annealing of each concentration.[21] The advantage of this method is to search the ground-state structure at each concentration efficiently. Furthermore, the final ground-state structures are verified by DFT calculations. After obtaining the stable slabs, the most stable absorption sites are further searched for each slab. Finally, a kinetic model is applied to calculate the activity of CO_2RR, and a large number of candidates with catalytic activities better than that of PdH(111) are found. The selectivities are analyzed to see if they are suitable for producing syngas.

2 Computational details

All DFT calculations are performed using the atomic simulation environment (ASE)[22,23] with the Vienna Ab initio Simulation Package (VASP) with the projector augmented wave (PAW) method.[24–26] The exchange and correlation functional used in this work is the Bayesian error estimation functional with van der Waals correlation (BEFF-vdW) ensemble.[27] The cutoff energy is set to 400 eV and the electronic smearing width is 0.05 eV. A Monkhorst-Pack grid of $3 \times 3 \times 1$ is used to sample the first Brillouin zone.[28] The electronic relaxation is set to stop when the energy difference between two steps is smaller than 10^{-6} eV. The ionic relaxation will converge when all the forces' norms are less than 0.01 eV $Å^{-1}$. The $Pd_xM_{1-x}H_y$ (111) surface is utilized because PdH (111) surface is the most stable in experiments (M is the metal element Ti or Nb).[17] To remove the electrostatic dipole-dipole interaction in the z direction due to periodic boundary conditions, a vacuum layer of approximately 15 Å is added, and the dipole correction is applied along the z direction. A 4×4 surface supercell cell of the $Pd_xM_{1-x}H_y$ (111) is utilized. Four atomic bilayers are used, each consisting of one Pd or M atomic layer (M is Ti or Nb element) and one H or X atomic layer (X denotes H vacancy). We fix the bottom two bilayers in their bulk positions when relaxing the slab.

The Cluster Expansion in the Atomic Simulation Environment software package (CLEASE) is used to implement cluster expansion (CE) calculations of the surface.[29] The initial slabs and corresponding relaxed energies are used to train the CE model, which can quickly predict the energies of the given new structures and thus greatly reduce the computational cost. The physical quantity (here it is the energy) of the material can be expressed as the following equation:[29,30]

$$q(\boldsymbol{\sigma}) = J_0 + \sum_{\alpha} m_\alpha J_\alpha \phi_\alpha \tag{1}$$

where $q(\boldsymbol{\sigma})$ is the energy of the configuration $\boldsymbol{\sigma}$. J_0 is the effective cluster interaction (ECI) of an

empty cluster. J_α denotes the ECI of cluster α, which needs to be fitted. m_α is the multiplicity factor that means the number of α per atom. ϕ_α denotes the correlation function of the cluster α, which is the average value of the cluster functions.[29] Up to 4-body clusters are included in this work, with the cutoff radii of 6.0, 5.0, 4.0 Å for 2-body, 3-body, and 4-body clusters, respectively. Monte Carlo Simulated Annealing (MCSA) is carried out to find the ground-state structure at each concentration. 65×65 MCSAs are implemented in parallel for each active learning iteration (65 H concentrations and 65 metal (Ti or Nb) concentrations in this work). Each MCSA uses standard Metropolis Monte Carlo at decreasing temperatures of 10^{10}, 10000, 6000, 4000, 2000, 1500, 1000, 800, 700, 600, 500, 400, 350, 300, 250, 200, 150, 100, 75, 50, 25, 2, and 1 K. 1000 Monte Carlo sweeps are set at each temperature and each sweep has N attempted swaps (N is the number of atoms in the cell). During the MCSA, the acceptance probability P_{acc} can be expressed as:[21,29]

$$P_{\text{acc}} = \min\left\{1, \exp\left(\frac{-\Delta E}{k_{\text{B}} T}\right)\right\}, \tag{2}$$

where ΔE is the energy difference between the new and the old structures. k_B denotes the Boltzmann constant and T is temperature in kelvin.

The binding energies, E_b, of adsorbates are calculated as:

$$E_b = E_{*+\text{ads}} - E_* - E_{\text{ads}}, \tag{3}$$

where $E_{*+\text{ads}}$ is the DFT energy of the surface with an adsorbate. E_* is the DFT energy of the clean surface, and E_{ads} is the DFT energy of the adsorbate. The adsorbates include HOCO*, CO*, OH*, and H*. The binding energy calculations of HOCO*, OH*, and H* are referenced to CO_2, H_2, and H_2O gas molecules, respectively, while that of CO* is referenced to CO gas molecule. The stabilization energy and zero point energy are considered when the OH* binding energy is calculated. The stabilization calculation details can be seen in Figure S18 and the corresponding description in the supporting information.

The mixing energy, E_{Mixing}, is calculated to obtain the convex hull of $Pd_xM_{1-x}H_y$ according to:

$$E_{\text{Mixing}} = E_{\text{Pd}_\text{x}\text{M}_{1-\text{x}}\text{H}_\text{y}} - x\mu_{\text{Pd(bulk)}} - (1-x)\mu_{\text{M(bulk)}} - y\frac{1}{2}\mu_{\text{H}_2\text{(g)}} \tag{4}$$

where $E_{\text{Pd}_\text{x}\text{M}_{1-\text{x}}\text{H}_\text{y}}$ is the DFT energy of $Pd_xM_{1-x}H_y$, where x is the concentration of element Pd and y is the concentration of element H. $\mu_{\text{Pd(bulk)}}$ and $\mu_{\text{M(bulk)}}$ denote the chemical potentials of bulk Pd and bulk metal M, respectively. $\mu_{\text{H}_2\text{(g)}}$ is the chemical potential of H_2 gas at 1 bar.

The CO_2RR elementary reactions and the corresponding net reaction rate equations of the kinetic model are considered:[17,20,31]

$$\text{CO}_2\text{(g)} + * + \text{H}^+ + \text{e}^- \longleftrightarrow \text{HOCO}* \tag{5}$$

$$\text{HOCO}* + \text{H}^+ + \text{e}^- \longleftrightarrow \text{CO}* + \text{H}_2\text{O(l)} \tag{6}$$

$$\text{CO}* \longleftrightarrow \text{CO(g)} + * \tag{7}$$

$$r_1 = k_1\theta_* p_{CO_2} - \frac{k_1}{K_1}\theta_{HOCO*} \tag{8}$$

$$r_2 = k_2\theta_{HOCO*} - \frac{k_2}{K_2}\theta_{CO*} \tag{9}$$

$$r_3 = k_3\theta_{CO*} - \frac{k_3}{K_3}\theta_* p_{CO} \tag{10}$$

k_1, k_2 and k_3 denote forward rate constants of equations 8, 9 and 10, respectively. K_1, K_2 and K_3 are the corresponding equilibrium constants. p_{CO_2} is the CO_2 partial pressure of 101 325 Pa. p_{CO} is the CO partial pressure of 5562 Pa. θ denotes the surface coverage.[8,11]

The HER elementary reactions are considered as:[32]

$$H^+ + e^- + * \longleftrightarrow H* \quad \text{(Volmer step)} \tag{11}$$

$$H* + H^+ + e^- \longleftrightarrow H_2(g) + * \quad \text{(Heyrovsky step)} \tag{12}$$

The Gibbs free energy (G) is calculated from:

$$G = E_{DFT} + E_{ZPE} + \int C_p dT - TS \tag{13}$$

where E_{DFT}, E_{ZPE}, C_p, and S are the DFT energy, the zero point energy, the heat capacity, and entropy, respectively. The free energy calculations of gas-phase species utilize the ideal gas approximation. The harmonic approximation is used to calculate the free energy of the slabs with adsorbate. The free energy calculations of HOCO*, CO*, OH*, and H* are references to CO_2 gas, H_2 gas, and liquid H_2O. A +0.15 eV correction per C=O, +0.15 eV correction for HOCO* and +0.1 eV correction for H_2 are used for systematic overbinding corrections with the BEEF-vdw functional in all calculations.[20,33] The free energy calculations of the molecules and various adsorbates can be found in Table S1 and Table S2, which are the same as in our previous work.[20] To avoid calculations of solvated protons, the computational hydrogen electrode (CHE) model is used in this work.[34]

3 Results and discussion

The workflow for the screening of stable and active candidates of $Pd_xM_{1-x}H_y$ for the CO_2RR can be divided into the following five stages. The first stage shows the search space of the slabs of each $Pd_xM_{1-x}H_y$. For the $4\times4\times4$ bare slabs, there are 64 metal sites, which can be occupied by either Pd or the metal M, and 64 hydrogen sites which can be occupied by H or be vacant. Thus, the search space (including symmetrically identical slabs) is $2^{64}\times2^{64} \approx 3.4\times10^{38}$, which is intractable to run DFT calculation for all slabs. To handle the huge search space, the ALCE model equipped with MCSA in parallel is utilized to obtain the ground-state slabs at each concentration. The specific implementation of the ALCE+MCSA can be seen in Figure S1. The ALCE can obtain the accurate surrogate model to speed up the CE energy prediction of the new given slabs, while MCSA is used to obtain the ground-state structures at each concentration quickly. During this

stage (the second stage), 100∼200 stable bare slabs are found according to the DFT convex hull, which is a huge reduction of search space from the original 3.4×10^{38} possible configurations. Since there are several unique adsorption sites for each stable bare surface, a local similarity comparison method is implemented to find unique sites.[21] After finding the unique adsorption sites, CO* adsorbate is added to the bare slabs, and its binding energies are calculated using DFT. During this stage (the third stage), 600∼900 unique slabs with CO* are found. The kinetic model in the fourth stage can be built to find the active range of CO* binding energies, reducing the number of possibly active slabs down to 200∼300. Because the number of slabs is limited at this point, the binding energies of HOCO*, OH*, and H* adsorbates can now be calculated via DFT. In the last stage, the final candidates can be found through the kinetic model dependent on the binding energies of CO* and HOCO* at the most stable adsorption sites. Finally, less than 30 stable and active candidates of $Pd_xM_{1-x}H_y$ are found. All structures for the final candidates with adsorbates can be found in our database.[35]

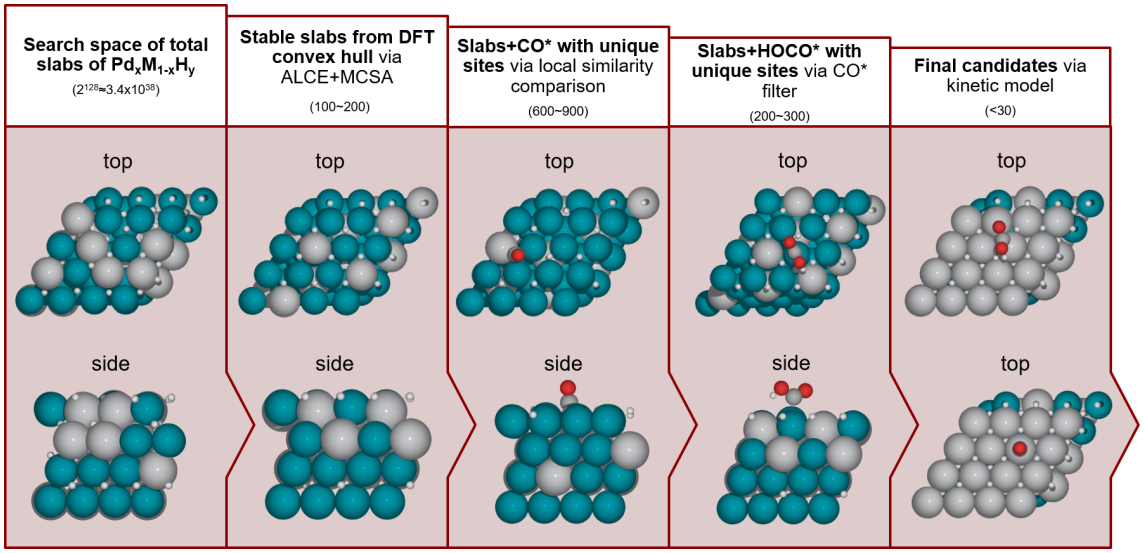

Figure 1: The workflow of the processes of the screening stable and active candidates of $Pd_xM_{1-x}H_y$ for CO_2RR. The top and side views of an example structure are given for the first 4 stages. The top views of HOCO* and CO* of an example candidate for the last stage. The blue spheres are Pd atoms, and the big grey spheres are metal M atoms (e.g., Ti). The white spheres are H atoms. The small grey spheres in adsorbates are C atoms, and the red spheres are O atoms.

To quickly and accurately obtain the energies of slabs, a good surrogate model is very important. Here, The ALCE method is carried out to train the CE model. The CE candidates are extracted from the CE convex hull and calculated by DFT and then added to the train set of the CE. We re-train the CE model with the new train set and then get new CE candidates from the new CE convex hull. During this process, we focus on the DFT convex hull of each iteration rather than the CE convex hull, which means the CE convex hull will be confirmed by DFT, and thus, the DFT

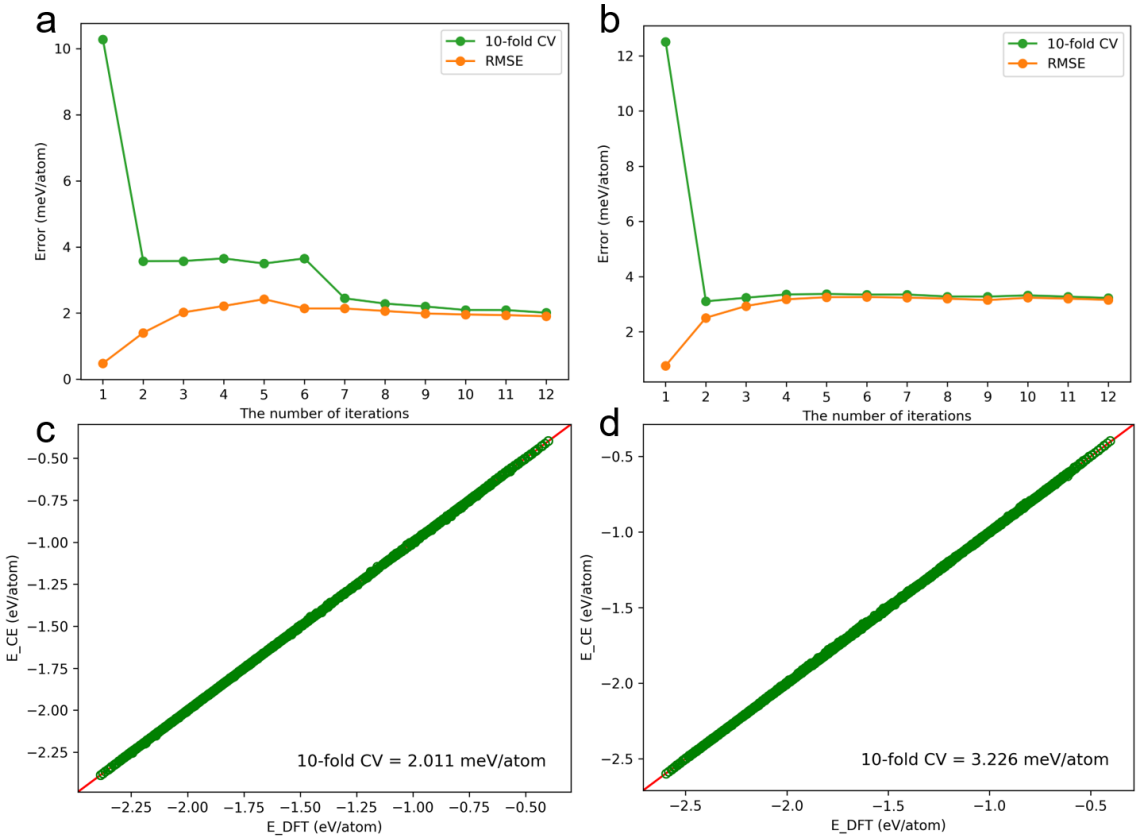

Figure 2: The 10-fold CV or RMSE as a function of ALCE iterations for $Pd_xTi_{1-x}H_y$ (a) and $Pd_xNb_{1-x}H_y$ (b). The linear fitting plots of CE energy and DFT energy of ALCE iteration 12 for (c) $Pd_xTi_{1-x}H_y$ and (d) $Pd_xNb_{1-x}H_y$.

convex hull is more reliable. This differs from other approaches that directly use the convex hull predicted from the surrogate model. As are shown in Figure 2a and Figure 2b, both $Pd_xTi_{1-x}H_y$ and $Pd_xNb_{1-x}H_y$ have 12 ALCE iterations. The green curves are 10-fold cross validation (CV) errors that we mainly focus on. The initial 10-fold CV error of $Pd_xTi_{1-x}H_y$ is 10.276 meV/atom as shown in Figure S2, which is a large error because only 50 random structures are in the initial train set. During the process of ALCE, the new structures of 50, 50, 200, 406, 500, 528, 382, 339, 320, 312, and 279 are added into the train set from iteration 2 to iteration 12, respectively. Their fitting plots can be found in Figure S3, Figure S4 and Figure S5. The 10-fold CV is gradually decreased and finally maintains stable at around 2.0 meV/atom as seen in Figure 2c. A similar case is observed for $Pd_xNb_{1-x}H_y$ in Figure 2b. Its initial 10-fold CV error is as large as 10.276 meV/atom as shown in Figure S20. Then, we add the new structures of 488, 499, 546, 575, 444, 437, 373, 272, 321, 342, and 352 into the train set from iteration 2 to iteration 12, respectively. The 10-fold CV error drop rapidly since iteration 2 and then remain stable at about 3.2 meV/atom, where the fitting plots can be seen in Figure S21, Figure S22, Figure S23, and Figure 2d. Besides, the orange curves in Figure 2a and Figure 2b are the RMSEs of only train sets (without test sets) for

$Pd_xTi_{1-x}H_y$ and $Pd_xNb_{1-x}H_y$. They are very small at first and then gradually go up to stable values, and finally, the RMSEs are close to their 10-fold CV errors. This could be because the overfitting is very large at first and gradually decreases as more structures are added to the train set.

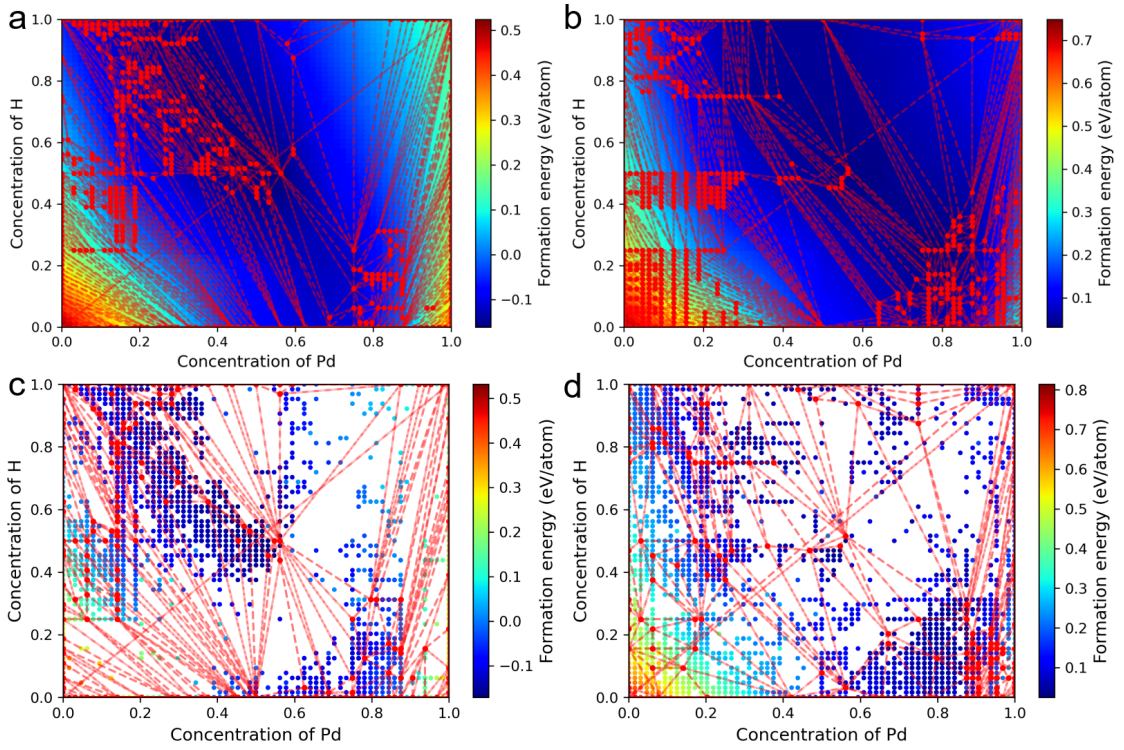

Figure 3: The CE convex hull plots of ALCE iteration 12 for (a) $Pd_xTi_{1-x}H_y$ and (b) $Pd_xNb_{1-x}H_y$. The DFT convex hull plots of ALCE iteration 12 for (c) $Pd_xTi_{1-x}H_y$ and (d) $Pd_xNb_{1-x}H_y$.

To identify stable compositions of $Pd_xTi_{1-x}H_y$ and $Pd_xNb_{1-x}H_y$, their CE and DFT convex hull plots are calculated. Before obtaining the CE convex hull, the most stable slabs at each unique H and Pd concentration are first calculated by MCSA. Since there are 65×65 unique concentrations, MCSAs at each concentration are implemented to get 65×65 stable slabs, which can be used to calculate CE convex hull. The points on the vertices of the CE convex hull are likely to be stable compositions considering the uncertainty of the CE model. The possible stable candidates from the CE convex hull need to be verified by the DFT convex hull. To better understand the shape of the convex hull for $Pd_xTi_{1-x}H_y$ and $Pd_xNb_{1-x}H_y$, their 3D CE convex hulls in iteration 12 are displayed in the Figure S13 and Figure S31. However, in order to clearly see the specific concentrations of the convex hull, the 2D convex hulls are used in the following. Figure 3a and Figure 3b show the CE convex hull plots of the ALCE final iteration 12 for $Pd_xTi_{1-x}H_y$ and $Pd_xNb_{1-x}H_y$, respectively. The CE convex hull of iteration 1-11 of $Pd_xTi_{1-x}H_y$ can be found in Figure S10, Figure S11 and Figure S12, while that of $Pd_xNb_{1-x}H_y$ can be found in Figure S28, Figure S29 and Figure S30. We notice that the CE convex hull of the last iteration is quite

different from the initial one, but that of the last several iterations are very similar. This is because the CE model in the beginning is not good enough, and the overfitting is very large. However, the CE model is eventually improved and there is almost no overfitting in the end. It is worth pointing out that this situation is more obvious for the DFT convex hull. Figure 3c and Figure 3d display the DFT convex hull plots of the ALCE in iteration 12 for $Pd_xTi_{1-x}H_y$ and $Pd_xNb_{1-x}H_y$, respectively. The previous iterations 1-11 of the DFT convex hull of $Pd_xTi_{1-x}H_y$ are shown in Figure S6, Figure S7 and Figure S8, while that of the DFT convex hull for $Pd_xNb_{1-x}H_y$ are shown in Figure S24, Figure S25 and S26. Since there are very similar tendencies for $Pd_xTi_{1-x}H_y$ and $Pd_xNb_{1-x}H_y$, we only take $Pd_xTi_{1-x}H_y$ as an example here. We can notice that the DFT convex hull shapes greatly differ in the first 5 iterations. After that, their shapes become quite similar. Especially the DFT convex hulls for the last 3 iterations are almost identical and thus we conclude that the DFT convex hull is converged. Furthermore, the volume of the DFT convex hull is a more straightforward quantity to understand whether the convex hull is converged. As shown in Figure S9 and S27, we can see that the volume of the DFT convex hull is rapidly going up in the first 5 iterations and finally reaches a stable maximum in the last several iterations, which further verify the converged DFT convex hull. However, we should clarify that it is very difficult to ensure that all the global ground state structures are located for any model at 65×65 concentrations. Even though our ALCE method with MCSA makes DFT convex hull converged, there still exists the rare probability that the true global ground state structures are not found, but the number of them is so few that we do not consider them. Finally, we find 125 stable slabs for $Pd_xTi_{1-x}H_y$ and 116 stable slabs for $Pd_xNb_{1-x}H_y$, which has greatly reduce the search space.

In order to further study the CO_2RR activity of $Pd_xTi_{1-x}H_y$ and $Pd_xNb_{1-x}H_y$, a kinetic model is built as illustrated in Equation 8, Equation 9 and Equation 10. As shown in Figure 4a and Figure 4c, the activity volcano plots of the $Pd_xTi_{1-x}H_y(111)$ and the $Pd_xNb_{1-x}H_y(111)$ depend on the binding energies of CO* and HOCO* and the color bars show the current density calculated by the kinetic model at $-0.5\,\mathrm{V}$ overpotential. The white dots in the Figures are all candidates after screening by the CO* filter in stage 4 in Figure 1, and $Pd_xTi_{1-x}H_y(111)$ has 111 candidates and $Pd_xNb_{1-x}H_y(111)$ has 76 candidates. The red dot is the slab of $Pd_{64}H_{64}$, about $3.7\,\mu\mathrm{A\,cm^{-2}}$, used for the comparison. It can be noticed that there are lots of candidates with better CO_2RR activity than that $Pd_{64}H_{64}$ for the $Pd_xTi_{1-x}H_y(111)$ in Figure 4a and they can be seen in the black dashed rectangle. For the $Pd_xTi_{1-x}H_y(111)$, 24 active candidates can be found in detail in the partial magnification in Figure 4b, which can be divided into four categories. The dots marked by blue has comparable current densities (3.7-4.2 $\mu\mathrm{A\,cm^{-2}}$) compared to the pure $Pd_{64}H_{64}$; the current densities of the dots marked by red, yellow, and black are sequentially better than that of $Pd_{64}H_{64}$. Especially, the current densities of the $Pd_{15}Ti_{49}H_{64}$ and $Pd_{12}Ti_{52}H_{60}$ can reach at about $5.1\,\mu\mathrm{A\,cm^{-2}}$ that is significant greater than $Pd_{64}H_{64}$. There is no too strong OH* binding on these active candidates as shown in Figure S16 and thus no OH* poisoning.

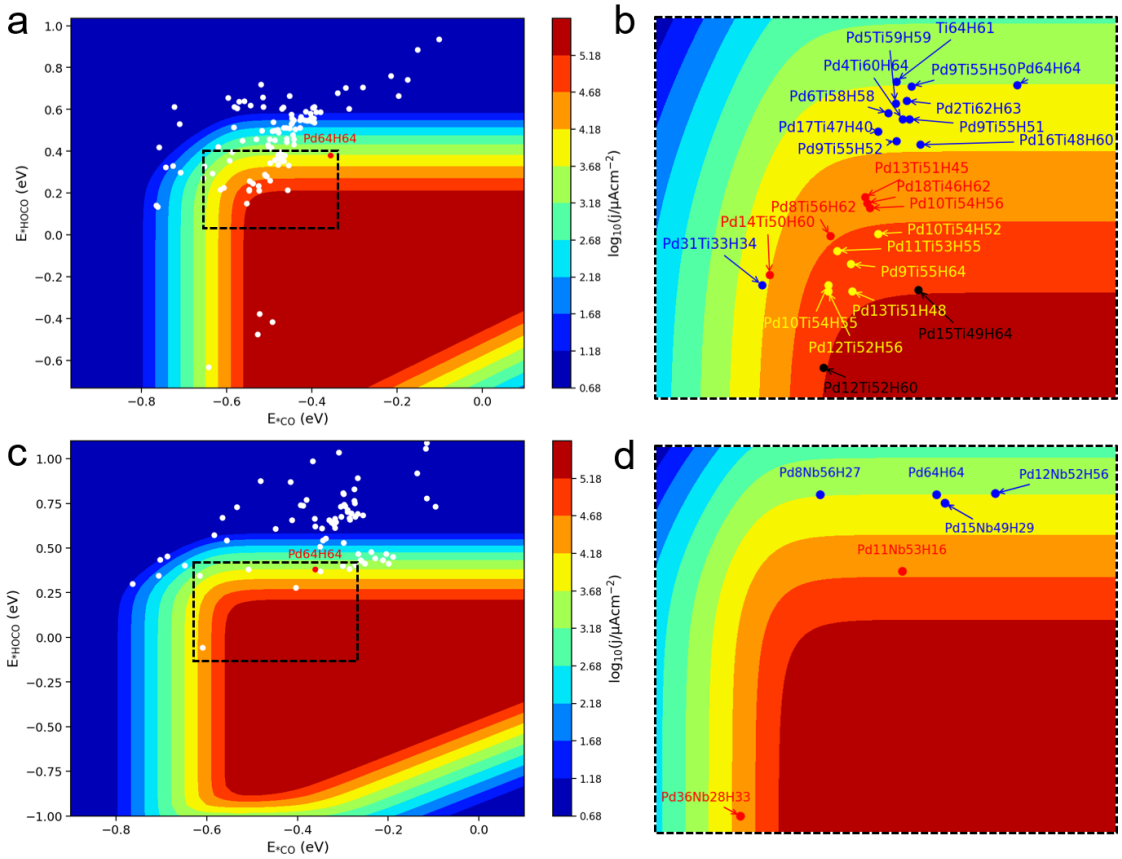

Figure 4: Activity volcano plot of (a) the $Pd_xTi_{1-x}H_y(111)$ candidates and (b) the corresponding partial magnification of black dashed area for CO_2RR at $-0.5\,V$ overpotential. Activity volcano plot of (c) the $Pd_xNb_{1-x}H_y(111)$ candidates and (d) the corresponding partial magnification of black dashed area for CO_2RR at $-0.5\,V$ overpotential.

Besides, it can be noticed that the active candidates have a higher concentration of Ti and H. For the $Pd_xNb_{1-x}H_y(111)$, there are fewer active candidates, only 5 comparable slabs, which are shown in the partial magnification Figure 4d. They are $Pd_8Nb_{56}H_{27}$, $Pd_{12}Nb_{52}H_{56}$, $Pd_{15}Nb_{49}H_{29}$, $Pd_{36}Nb_{28}H_{33}$ and $Pd_{11}Nb_{53}H_{16}$, which have high Nb concentraion. Especially, the $Pd_{11}Nb_{53}H_{16}$ has the highest current density, $4.6\,\mu A\,cm^{-2}$. The OH* binding on these active candidates are not too strong and thus do not poison the surfaces as shown in Figure S34. Besides, it is worth mentioning that the candidates of the Pd alloy hydride have much better CO_2RR activity than the corresponding candidates of the doped Pd hydride in our previous work.[20]

In order to further understand the catalytic activities of active $Pd_xTi_{1-x}H_y$ and $Pd_xNb_{1-x}H_y$ candidates, the free energy diagrams of the CO_2RR and HER are shown in Figure 5. The black curves in all Figures are the free energy diagram of pure $Pd_{64}H_{64}$, which is used as a reference. The CO_2RR free energy diagrams in Figure 5a and Figure 5c illustrate that the HOCO* step of $Pd_{64}H_{64}$ is the potential limiting step, which means the free energy of the HOCO* is too high and

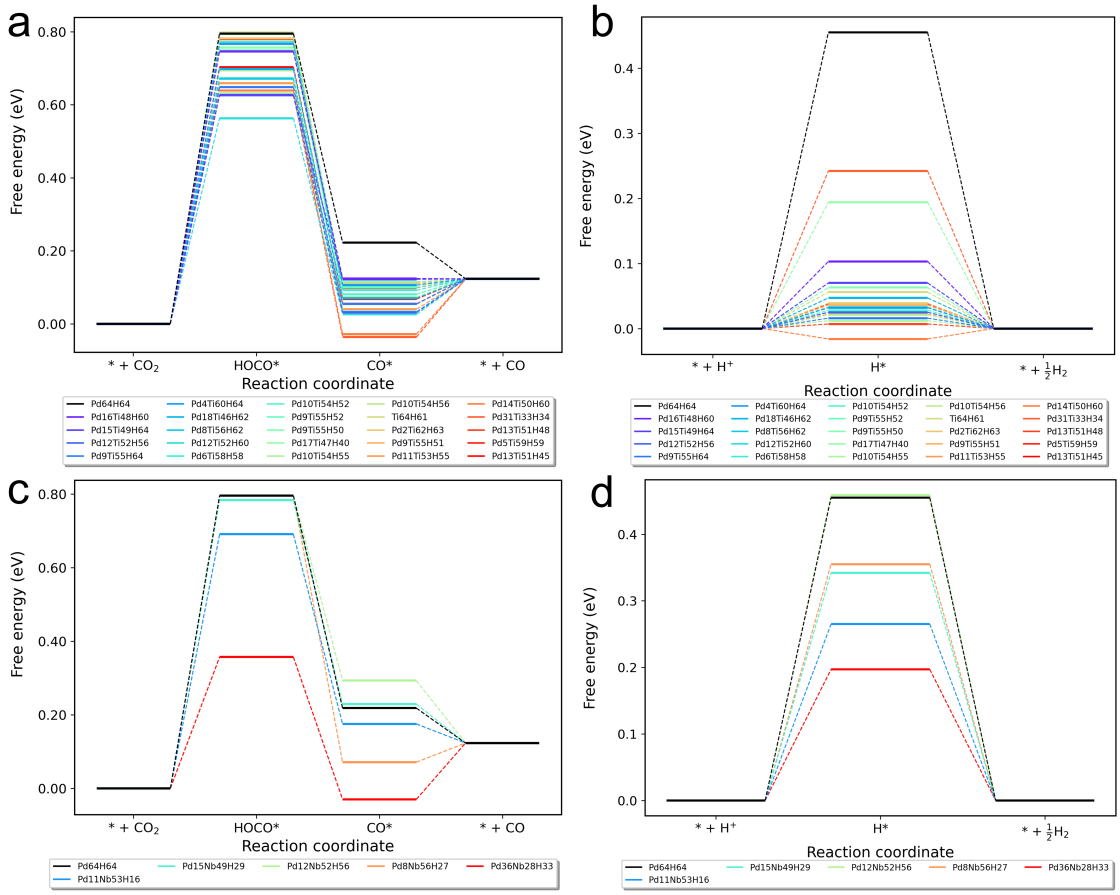

Figure 5: Free energy diagram of (a) CO_2RR and (b) HER of active candidates for the $Pd_xTi_{1-x}H_y(111)$. Free energy diagram of (c) CO_2RR and (d) HER of active candidates for the $Pd_xNb_{1-x}H_y(111)$.

thus the HOCO* binding is too weak to form efficiently on the surface. We notice that all of the HOCO* steps of the active candidates are lower than that of $Pd_{64}H_{64}$, which results in stronger HOCO* binding on the surface and thus make the reaction 5 easier. Besides, it can be noticed that the majority of active candidates have a stronger binding of CO* than $Pd_{64}H_{64}$, but the binding energy should not be too strong to avoid CO* poisoning. The CO_2RR free energy diagrams of all candidates at stage 4 in Figure 1 are also displayed in Figure S14 and Figure S32, most of them are inactive for both $Pd_xTi_{1-x}H_y$ and $Pd_xNb_{1-x}H_y$. This is because either their HOCO* step is so high (the binding is too weak) that it is too difficult to produce HOCO*, or the CO* step is too low (the binding is too strong)causing CO* poisoning. For the $Pd_{15}Ti_{49}H_{64}$, $Pd_{12}Ti_{52}H_{60}$, and $Pd_{11}Nb_{53}H_{16}$ with high current densities, their HOCO* binding is not weak and the CO* binding is not strong, which is the reason why they are very active. However, the HER free energy diagrams for both $Pd_xTi_{1-x}H_y$ and $Pd_xNb_{1-x}H_y$ indicate that the candidates that are active for CO_2RR also have better HER performance than $Pd_{64}H_{64}$ as shown Figure 5b and Figure 5d. All of them have lower free energy of the Volmer step compared to the $Pd_{64}H_{64}$, which can improve

their HER activity. The HER free energy diagrams of all candidates at stage 4 in Figure 1 are also given in Figure S15 and Figure S33. We notice that most candidates have stronger binding of H* than $Pd_{64}H_{64}$ and the bindings are not strong, which leads to their high HER activity. However, the candidates with high concentrations of H and Pd have weaker binding of H* than $Pd_{64}H_{64}$ and thus lower HER activity, which is consistent with our previous work.[21] In addition, there are no obvious scaling relations between the binding energies of different adsorbates for both $Pd_xTi_{1-x}H_y$ and $Pd_xNb_{1-x}H_y$ as shown in Figure S16 and Figure S34, which may be attributed to the high complexity of the composition of the surfaces and the different stable adsorption sites. Figure S19 and Figure S36 describe the selectivity of all candidates toward CO and H_2 for $Pd_xTi_{1-x}H_y$ and $Pd_xNb_{1-x}H_y$, where $\Delta G_{HOCO*} - \Delta G_{H*}$ is used as a descriptor to illustrate the tendency towards CO_2RR and HER. The more positive value of $\Delta G_{HOCO*} - \Delta G_{H*}$ tends to generate more H_2, while the more negative value will produce more CO_2. It can be seen that a majority of candidates can produce more H_2 than CO_2 and only a small part of candidates can generate more CO_2.

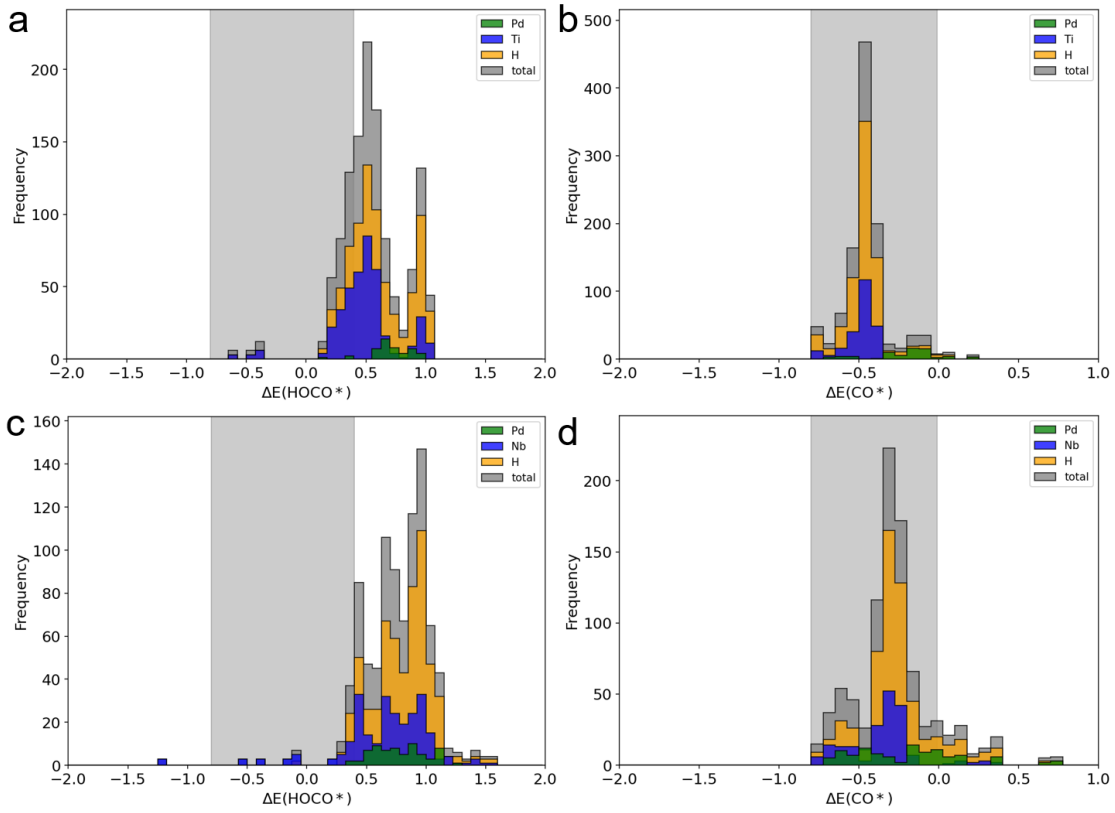

Figure 6: Distribution of atom Pd, Ti, and H of all candidates within the cutoff sphere as a function of (a) the HOCO* and (b) the CO* binding energies. Distribution of atom Pd, Nb, and H of all candidates within the cutoff sphere as a function of (c) HOCO* and (d) CO* binding energies.

To further reveal the role of each element in affecting the binding energies, the statistical distributions of the binding energy of different adsorbates as a function of the frequency of appearance of

each element in a local environment are displayed in Figure 6. The grey rectangle area is the active zone for HOCO* or CO* according to the kinetic model for CO production. Figure 6a and Figure 6b are the distributions of the binding energies of HOCO* and CO* for $Pd_xTi_{1-x}H_y$. Most of the HOCO* binding energies are not in the active zone, and only a small part of elements Ti and H is distributed in this active zone. However, the center of the CO* binding energies is nearly in the middle of the active zone. The distributions of the OH* and H* binding energies for $Pd_xTi_{1-x}H_y$ are also shown in Figure S17. It is worth pointing out that Pd is distributed in the weak binding zone of the HOCO*, CO*, and OH*, which implies that Pd may weaken their binding. This is not the case for H* distribution as the element Pd is mainly distributed in the center of the zone of the H* binding energies. For the $Pd_xNb_{1-x}H_y$, the distributions of binding energies of HOCO*, CO*, OH* and H* are displayed in Figure 6c-d and Figure S35a-b, respectively. Similar to the $Pd_xTi_{1-x}H_y$, most of the binding energies of the HOCO* are higher than the active zone, and only a tiny part of Ti and H is in the HOCO* active zone. The centers of the distributions for the element Pd, Nb, and H are roughly in the middle of the CO* binding. Their OH* and H* distributions are displayed in Figure S34. The metal element Pd is obviously only in the weak binding zone of the OH* (1.0-2.0 eV), while element Nb is mainly in the strong binding zone of the OH*. This means element Pd may weaken the OH* binding. Pd is mainly distributed in the strong binding zone of the H*. It is worth noting that the frequency of occurrence of element Pd is very low within the local spheres for both $Pd_xTi_{1-x}H_y$ and $Pd_xNb_{1-x}H_y$, which is much lower than that of Ti/Nb and H. This indicates that the adsorbates binding to elements Ti/Nb and H mainly contribute to the binding energy of the candidates.

4 Conclusions

We have used a surrogate model ALCE+MCSA, a CO* filter, and kinetic model to screen high-performance catalysts of alloy hydrides of $Pd_xTi_{1-x}H_y$ and $Pd_xNb_{1-x}H_y$ for CO_2RR, which greatly reduces the massive search space. Due to the large complexity that includes different compositions of alloy hydrides, different concentrations of metal elements and H of alloy hydrides, different adsorption sites, and different adsorbates, it is impossible to find the stable and active catalysts only using the density functional theory calculation. We utilize the high precision and low overfitting ALCE model with RMSE of about 2 or 3 meV/atoms, and a large amount of MCSA to identify the ground state Pd alloy hydride surfaces from the convex hull. Adsorption sites and binding energies of adsorbates are also accurate as they are also calculated from DFT. Finally, 24 active candidates of $Pd_xTi_{1-x}H_y$ and 5 active candidates of $Pd_xNb_{1-x}H_y$ are screened out according to the kinetic model. Especially, the $Pd_{15}Ti_{49}H_{64}$ ($Pd_{0.23}Ti_{0.77}H$), $Pd_{12}Ti_{52}H_{60}$ ($Pd_{0.19}Ti_{0.81}H_{0.94}$) and $Pd_{11}Nb_{53}H_{16}$ ($Pd_{0.17}Nb_{0.83}H_{0.25}$) have good stability and excellent current densities, which are approximate 5.1, 5.1 and 4.6 $\mu A\,cm^{-2}$, respectively, and they are greatly higher than that of $Pd_{64}H_{64}$ at 3.7 $\mu A\,cm^{-2}$. These are because their HOCO* binding is not too weak, and CO*

binding is not too strong. Consequently, three candidates $Pd_{0.23}Ti_{0.77}H$, $Pd_{0.19}Ti_{0.81}H_{0.94}$ and $Pd_{0.17}Nb_{0.83}H_{0.25}$ are recommended for further experimental investigations.

Data availability

The data including all DFT structures with the adsorbates HOCO*, CO*, H* and OH* on all adsorption sites in this work are availabe at DTU database https://data.dtu.dk: `https://doi.org/10.11583/DTU.23798751`

Code availability

All plot, pre-processing, and post-processing codes in this paper are available at the following Gitlab repository named Pcat: `https://gitlab.com/changzhiai/pcat`.

Acknowledgments

This work was supported by the China Scholarship Council and by the Villum Foundation through the research center V-Sustain (#9455). The authors thank the Niflheim Linux supercomputer cluster at the Department of Physics at the Technical University of Denmark.

Keywords

CO_2 reduction; $Pd_xM_{1-x}H_y$; Complex hydrides; High-throughput screening; Active learning; Cluster expansion; Kinetic activity; Selectivity.

References

[1] I. Stavi, *All Earth* **2023**, *35*, 38–45.

[2] S. Solomon, G.-K. Plattner, R. Knutti, P. Friedlingstein, *Proceedings of the National Academy of Sciences* **2009**, *106*, 1704–1709.

[3] S. Nitopi, E. Bertheussen, S. B. Scott, X. Liu, A. K. Engstfeld, S. Horch, B. Seger, I. E. L. Stephens, K. Chan, C. Hahn, J. K. Nørskov, T. F. Jaramillo, I. Chorkendorff, *Chem. Rev.* **2019**, *119*, 7610–7672.

[4] Y. A. Alli, P. O. Oladoye, O. Ejeromedoghene, O. M. Bankole, O. A. Alimi, E. O. Omotola, C. A. Olanrewaju, K. Philippot, A. S. Adeleye, A. S. Ogunlaja, *Science of The Total Environment* **2023**, *868*, 161547.

[5] H.-R. M. Jhong, S. Ma, P. J. Kenis, *Current Opinion in Chemical Engineering* **2013**, *2*, 191–199.

[6] S. Chu, Y. Cui, N. Liu, *Nature Materials* **2016**, *16*, 16–22.

[7] S. J. Davis, N. S. Lewis, M. Shaner, S. Aggarwal, D. Arent, I. L. Azevedo, S. M. Benson, T. Bradley, J. Brouwer, Y.-M. Chiang, C. T. M. Clack, A. Cohen, S. Doig, J. Edmonds, P. Fennell, C. B. Field, B. Hannegan, B.-M. Hodge, M. I. Hoffert, E. Ingersoll, P. Jaramillo, K. S. Lackner, K. J. Mach, M. Mastrandrea, J. Ogden, P. F. Peterson, D. L. Sanchez, D. Sperling, J. Stagner, J. E. Trancik, C.-J. Yang, K. Caldeira, *Science* **2018**, *360*.

[8] Y. Hori, A. Murata, R. Takahashi, *J. Chem. Soc. Faraday Trans. 1* **1989**, *85*, 2309.

[9] F. Pan, Y. Yang, *Energy & Environmental Science* **2020**, *13*, 2275–2309.

[10] X. Zhang, Z. Zhang, H. Li, R. Gao, M. Xiao, J. Zhu, M. Feng, Z. Chen, *Advanced Energy Materials* **2022**, *12*, 2201461.

[11] A. A. Peterson, F. Abild-Pedersen, F. Studt, J. Rossmeisl, J. K. Nørskov, *Energy Environ. Sci.* **2010**, *3*, 1311.

[12] G.-R. Zhang, S.-D. Straub, L.-L. Shen, Y. Hermans, P. Schmatz, A. M. Reichert, J. P. Hofmann, I. Katsounaros, B. J. M. Etzold, *Angewandte Chemie International Edition* **2020**, *59*, 18095–18102.

[13] Y. Hori in *Modern Aspects of Electrochemistry*, *Vol. 42*, Springer New York, **2008**, pp. 89–189.

[14] D. Xu, K. Li, B. Jia, W. Sun, W. Zhang, X. Liu, T. Ma, *Carbon Energy* **2022**, *5*.

[15] B. Wu, J. Chen, L. Qian, *Catalysts* **2022**, *12*, 860.

[16] W. Sheng, S. Kattel, S. Yao, B. Yan, Z. Liang, C. J. Hawxhurst, Q. Wu, J. G. Chen, *Energy Environ. Sci.* **2017**, *10*, 1180–1185.

[17] W. Zhu, S. Kattel, F. Jiao, J. G. Chen, *Adv. Energy Mater.* **2019**, *9*, 1802840.

[18] Y. Liu, D. Tian, A. N. Biswas, Z. Xie, S. Hwang, J. H. Lee, H. Meng, J. G. Chen, *Angewandte Chemie International Edition* **2020**, *59*, 11345–11348.

[19] J. H. Lee, S. Kattel, Z. Jiang, Z. Xie, S. Yao, B. M. Tackett, W. Xu, N. S. Marinkovic, J. G. Chen, *Nature Communications* **2019**, *10*.

[20] C. Ai, T. Vegge, H. A. Hansen, *ChemSusChem* **2022**, *15*, 202200008.

[21] C. Ai, J. Chang, A. Tygesen, T. Vegge, H. A. Hansen, **2023**, DOI 10.26434/chemrxiv-2023-kkk48.

[22] A. H. Larsen, J. J. Mortensen, J. Blomqvist, I. E. Castelli, R. Christensen, M. Dułak, J. Friis, M. N. Groves, B. Hammer, C. Hargus, E. D. Hermes, P. C. Jennings, P. B. Jensen, J. Kermode, J. R. Kitchin, E. L. Kolsbjerg, J. Kubal, K. Kaasbjerg, S. Lysgaard, J. B. Maronsson, T. Maxson, T. Olsen, L. Pastewka, A. Peterson, C. Rostgaard, J. Schiøtz, O. Schütt, M. Strange, K. S. Thygesen, T. Vegge, L. Vilhelmsen, M. Walter, Z. Zeng, K. W. Jacobsen, *J. Phys.: Condens. Matter* **2017**, *29*, 273002.

[23] S. Bahn, K. Jacobsen, *Comput. Sci. Eng.* **2002**, *4*, 56–66.

[24] G. Kresse, J. Hafner, *Phys. Rev. B* **1993**, *47*, 558–561.

[25] G. Kresse, J. Furthmüller, *Phys. Rev. B* **1996**, *54*, 11169–11186.

[26] P. E. Blöchl, *Phys. Rev. B* **1994**, *50*, 17953–17979.

[27] J. Wellendorff, K. T. Lundgaard, A. Møgelhøj, V. Petzold, D. D. Landis, J. K. Nørskov, T. Bligaard, K. W. Jacobsen, *Phys. Rev. B* **2012**, *85*.

[28] H. J. Monkhorst, J. D. Pack, *Phys. Rev. B* **1976**, *13*, 5188–5192.

[29] J. H. Chang, D. Kleiven, M. Melander, J. Akola, J. M. Garcia-Lastra, T. Vegge, *Journal of Physics: Condensed Matter* **2019**, *31*, 325901.

[30] D. D. Fontaine in *Solid State Physics*, Elsevier, **1994**, pp. 33–176.

[31] H. A. Hansen, J. B. Varley, A. A. Peterson, J. K. Nørskov, *J. Phys. Chem. Lett.* **2013**, *4*, 388–392.

[32] J. K. Nørskov, T. Bligaard, A. Logadottir, J. R. Kitchin, J. G. Chen, S. Pandelov, U. Stimming, *J. Electrochem. Soc.* **2005**, *152*, J23.

[33] R. Christensen, H. A. Hansen, T. Vegge, *Catal. Sci. Technol.* **2015**, *5*, 4946–4949.

[34] J. K. Nørskov, J. Rossmeisl, A. Logadottir, L. Lindqvist, J. R. Kitchin, T. Bligaard, H. Jønsson, *J. Phys. Chem. B* **2004**, *108*, 17886–17892.

[35] C. Ai, J. H. Chang, A. S. Tygesen, T. Vegge, H. A. Hansen, High-throughput screening of complex hydrides $Pd_xM_{1-x}H_y$ on CO_2 reduction, https://doi.org/10.11583/DTU.23798751.